Revealing the atomic ordering of binary intermetallics using in situ heating techniques at multilength scales

Yin Xiong[a,1], Yao Yang[a,1], Howie Joress[b,c,1], Elliot Padgett[d], Unmukt Gupta[e], Venkata Yarlagadda[f], David N. Agyeman-Budu[b,c], Xin Huang[b], Thomas E. Moylan[f], Rui Zeng[a], Anusorn Kongkanand[f], Fernando A. Escobedo[e], Joel D. Brock[b,d], Francis J. DiSalvo[a,2], David A. Muller[d,g,2], and Héctor D. Abruña[a,2]

[a]Department of Chemistry and Chemical Biology, Baker Laboratory, Cornell University, Ithaca, NY 14853; [b]Cornell High Energy Synchrotron Source, Cornell University, Ithaca, NY 14850; [c]Department of Materials Science and Engineering, Cornell University, Ithaca, NY 14850; [d]School of Applied and Engineering Physics, Cornell University, Ithaca, NY 14853; [e]Robert Frederick Smith School of Chemical and Biomolecular Engineering, Cornell University, Ithaca, NY 14853; [f]Fuel Cell R&D, General Motors Global Propulsion Systems, Pontiac, MI 48340; and [g]Kavli Institute at Cornell for Nanoscale Science, Cornell University, Ithaca, NY 14853

Contributed by Héctor D. Abruña, December 14, 2018 (sent for review September 10, 2018; reviewed by Plamen Atanassov, Marc Koper, and Eugene S. Smotkin)

Ordered intermetallic nanoparticles are promising electrocatalysts with enhanced activity and durability for the oxygen-reduction reaction (ORR) in proton-exchange membrane fuel cells (PEMFCs). The ordered phase is generally identified based on the existence of superlattice ordering peaks in powder X-ray diffraction (PXRD). However, after employing a widely used postsynthesis annealing treatment, we have found that claims of "ordered" catalysts were possibly/likely mixed phases of ordered intermetallics and disordered solid solutions. Here, we employed in situ heating, synchrotron-based, X-ray diffraction to quantitatively investigate the impact of a variety of annealing conditions on the degree of ordering of large ensembles of Pt_3Co nanoparticles. Monte Carlo simulations suggest that Pt_3Co nanoparticles have a lower order–disorder phase transition (ODPT) temperature relative to the bulk counterpart. Furthermore, we employed microscopic-level in situ heating electron microscopy to directly visualize the morphological changes and the formation of both fully and partially ordered nanoparticles at the atomic scale. In general, a higher degree of ordering leads to more active and durable electrocatalysts. The annealed Pt_3Co/C with an optimal degree of ordering exhibited significantly enhanced durability, relative to the disordered counterpart, in practical membrane electrode assembly (MEA) measurements. The results highlight the importance of understanding the annealing process to maximize the degree of ordering in intermetallics to optimize electrocatalytic activity.

in situ heating TEM | in situ heating XRD | ordered intermetallics | order–disorder phase transition | oxygen reduction reaction

Pt-based intermetallics display superior electrocatalytic activity for the normally sluggish oxygen-reduction reaction (ORR), as well as enable a decrease in Pt loading, compared with Pt/C, in proton exchange membrane (PEM) fuel cells (1–6). As-synthesized, Pt-based alloy (Pt-M; M = Mn, Fe, Co, Ni, etc.) nanoparticles (NPs) generally form as a disordered solid solution in which the occupancy of a given site by Pt or M atoms is random and without local preference. The probability of occupancy by Pt or M is determined only by the stoichiometric ratio of Pt and M in a particular particle. These alloys generally suffer from a rapid loss of activity during electrochemical cycling due to the oxidation and dissolution of the M element and subsequent changes in both the particle morphology and the crystal structure (7). In some systems, such as the Pt-Sn system, partially ordered intermetallic particles can be obtained at room temperature and further improved to fully ordered phase by low temperature annealing (200 °C) (8). However, in most other cases, postsynthesis annealing at high temperatures is required to transform the disordered solid solution phase into the ordered intermetallic phase. These intermetallic NPs show significantly better durability and improved electrocatalytic activity (9–29). The enhanced durability of ordered intermetallics can be attributed to a more stable structure, which arises from the stronger heteroatomic Pt-M bond and a greater enthalpy of formation relative to its disordered counterpart. Ordered Pt_3M intermetallics normally have a primitive cubic crystal structure ($AuCu_3$-type, Pm-3m), while ordered PtM intermetallics typically have a tetragonal crystal structure of the AuCu-type, P4/mmm. Because ordered intermetallics of Pt_3M and PtM have different crystal symmetry and additional atomic ordering, compared with their disordered counterparts, they show extra peaks in X-ray diffraction (XRD), which are usually referred to as superlattice ordering peaks.

In studies of ordered intermetallic catalysts, there are two related questions that are of particular interest: Is the ordered intermetallic phase present, and what is the phase fraction of the intermetallic? The first question can be quantitatively determined by the existence of superlattice ordering peaks in powder XRD (11–29). By measuring the relative intensity of the

Significance

We present a comprehensive quantitative study of the dynamic order–disorder phase transition of Pt_3Co nanoparticles, binary intermetallic oxygen-reduction reaction fuel cell electrocatalysts, during postsynthesis annealing. We employed in situ synchrotron-based X-ray diffraction (XRD) and in situ scanning transmission EM (STEM) to study the phase transition and morphological and structural changes during real-time annealing. In situ XRD revealed the impact of annealing/cooling conditions on the degree of ordering, particle size and lattice strain. In situ heating STEM enabled visualization of nanoparticle migration and growth. We find that a higher degree of ordering leads to more active and durable electrocatalysts. Our findings represent a groundbreaking advance in electrocatalyst development/design with a broad impact on energy materials, in general, and fuel cells, in particular.

Author contributions: Y.X., Y.Y., A.K., F.A.E., J.D.B., F.J.D., D.A.M., and H.D.A. designed research; H.J. designed the in situ heating setup; Y.X., Y.Y., H.J., E.P., U.G., V.Y., D.N.A.-B., X.H., T.E.M., and R.Z. performed research; Y.X., Y.Y., and H.J. performed the in situ heating XRD experiment; Y.Y. and E.P. performed the in situ heating TEM experiment; U.G. performed the Monte Carlo simulation; Y.X., Y.Y., H.J., and E.P. analyzed data; and Y.X., Y.Y., H.J., and E.P. wrote the paper.

Reviewers: P.A., University of California, Irvine; M.K., Leiden University; and E.S.S., Northeastern University.

The authors declare no conflict of interest.

[1]Y.X., Y.Y., and H.J. contributed equally to this work.

[2]To whom correspondence may be addressed. Email: hda1@cornell.edu, dm24@cornell.edu, or fjd3@cornell.edu.

This article contains supporting information online at www.pnas.org/lookup/suppl/doi:10.1073/pnas.1815643116/-/DCSupplemental.

superstructure peaks, information that is important but often neglected, the degree of ordering can be quantified. Having a measure of the degree of ordering is important to understand the intermetallic phase's contribution to catalyst performance and is necessary for understanding and optimizing the synthesis and annealing conditions.

After performing a systematic literature survey on ordered intermetallic NPs, which included the most common Pt-M and Pd-M intermetallics, we realized that most of these studies only qualitatively described the formation of ordered intermetallics, and further quantitative understanding of the degree of ordering was required (*SI Appendix*, Table S1) (11–29). For example, in our previous studies on Pt_3Co (2) and PdFe (6), intermetallic NPs were found to be only partially ordered, despite our attempts to optimize the postsynthesis annealing conditions. In our other studies on PtSn (8) and PdZn (20), intermetallic NPs were measured to be fully in the ordered phase. This suggests that it is likely that some claims of "ordered" intermetallic electrocatalysts may, in fact, be mixed phases of ordered intermetallic and disordered solid solution particles. It is possible that, due to high strain and surface energy, for some NP systems, and from a thermodynamic standpoint, only partial order can be achieved, even if a pure phase can be obtained at equilibrium in the bulk. In either case, the synthesized, disordered alloy needs to overcome energetic barriers and kinetics to nucleate and grow the more stable, ordered intermetallic phase through the annealing treatment. However, the annealing process must be carefully designed/controlled. The newly formed ordered intermetallic phase can revert back to the disordered phase if the temperature surpasses a critical, order–disorder phase transition (ODPT) temperature (T_c = 750 °C for bulk Pt_3Co) (30). The ODPT represents an intriguing process, coupling both kinetic and thermodynamic aspects. Further, nucleation and growth may also be (and likely are) influenced by the composition, morphology and size of each NP.

It is critical to understand the ODPT behavior of NPs, which will, in turn, enable us to develop better annealing processes to increase the degree of ordering of NP electrocatalysts and, by extension, enhance fuel cell performance. However, mechanistic studies of such processes have been challenging due to the lack of suitable in situ techniques capable of tracking the dynamic phase transition and structural changes of metastable intermediates under real-time annealing conditions. Previous studies have only involved in situ heating, during XRD, to study the lattice strain of Pt-Cu intermetallics (31), or have employed microscopic-level, in situ heating transmission EM (TEM), to investigate morphological changes of Pt (32) and Pt-based alloys (33–37). However, to the best of our knowledge, none of them has attempted to quantitatively study the degree of ordering using XRD and correlate it with the evolution of particle morphology and the formation of ordered intermetallics, at the atomic scale, using EM.

In this study, we have investigated the ODPT of Pt_3Co NPs during a temperature annealing treatment, using both in situ heating synchrotron-based XRD and in situ heating TEM. We have studied, quantitatively, the effects of annealing and cooling conditions (temperature and time) on the degree of ordering. We further employed in situ heating TEM to directly visualize the morphological and structural transition at the atomic-scale, during the thermal annealing treatment. Finally, we have systematically correlated catalyst durability to the degree of ordering, where a higher degree of ordering led to enhanced durability. This mechanistic study, involving both in situ heating XRD and in situ heating TEM, provides a microscopically detailed picture of postsynthesis processing.

Method

The Pt_3Co/C catalysts were prepared by an impregnation method in which Pt and Co metal precursors were reduced at 300 °C under forming gas to form disordered alloy. Postannealing treatment was applied at a series of temperatures to transform Pt_3Co/C into partially ordered intermetallics. Electrochemical ORR measurements were carried out using a rotating disk electrode (RDE) (Pine Instruments) in an oxygen-saturated 0.1 M $HClO_4$ solution at a rotation rate of 1,600 rpm and a sweep rate of 5 mV/s. MEA tests were performed at 94 °C (H_2/air) using the synthesized Pt_3Co/C and Pt/C as the cathode and anode, respectively, and perfluorosulfonic acid as the membrane. The in situ XRD measurements were performed at the A1 station of the Cornell High Energy Synchrotron Source (CHESS) using a customized setup. The in situ heating TEM experiments were conducted in a FEI Tecnai F20 electron microscope at 200 keV with Protochips Aduro heating holder and E-AHA21 E-chip. Monte Carlo (MC) simulations were performed using N-body potentials, provide an efficient means to quickly simulate the equilibrium and kinetic properties of large atomic systems (~10,000 particles). More experimental details can be found in *SI Appendix*.

Results and Discussions

In Situ Heating Synchrotron-Based XRD. Pt_3Co/C disordered alloys were synthesized using an impregnation method (2) in which precursors were reduced under forming gas at 300 °C and the as-synthesized Pt_3Co/C catalysts were subsequently annealed further at high temperatures under forming gas. The XRD patterns of the as-synthesized Pt_3Co/C and Pt_3Co/C annealed at 700 °C in a conventional tube furnace were first measured in the in situ heating XRD stage to verify the reliability of the set-up (Fig. 1*A*). After annealing, the sample exhibited multiple superlattice ordering peaks: (100) at 23°, (110) at 32.5°, (210) at 53.5°, (211) at 59°, (300) at 74.3°, and (310) at 79°, which match well with the XRD reference of ordered intermetallic Pt_3Co [powder diffraction file (PDF) # 01-071-7410], confirming the formation of ordered phase.(Fig. 1*B*) In this experiment, the orientation of the crystallites should be random both at the NP level and within the NP/C mixture. Beyond this assumption, the data themselves provide assurance that the orientations of the crystallites are sufficiently random. First, data were collected using a 2D detector and integrated to generate the 1D data sets. The detector image of the as-prepared Pt_3Co intermetallic NPs collects a portion of the ring, as shown in *SI Appendix*, Fig. S1. It can be seen, particularly in the smallest ring, that there is no change in intensity as a function of position along the ring, indicating a random orientation of grains. After subtracting the background, by selecting three points to form the baseline (Fig. 1*C*, *Inset*), the XRD pattern was analyzed further to quantify the relative content of the ordered phase. We employed the intermetallic peak (110) at 32.5° for analysis. It is the second strongest intermetallic peak, yielding a sufficient signal-to-noise ratio for further analysis. While the strongest intermetallic peak is the (100), it is located within the diffuse scattering ring from the carbon support, making it difficult to accurately extract the integrated intensity of this peak, precluding an accurate intensity analysis. Because there is some overlap between the (111) and (200) peaks, due to the broadening of the peaks by the relatively small domain/crystallite size, the ratio of the integrated area under the (110) peak (red) to that of the sum of the areas under the (111) and (200) peaks (blue), $I_{(110)}/(I_{(111)} + I_{(200)})$, was used so as to yield a more accurate quantitative evaluation. The theoretical value of $I_{(110)}/(I_{(111)} + I_{(200)})$, based on the structure factor, for Pt_3Co is 0.078, as calculated using the XRD database of ordered Pt_3Co. This corresponds to a 100% of fully ordered intermetallic Pt_3Co particles (Fig. 1*D*). The relative fraction of the ordered phase exhibits a linear relationship with $I_{(110)}/(I_{(111)} + I_{(200)})$. This approach is valid since the intensity of the (111) and (200) peaks, the fundamental reflections, are constant for both ordered and disordered phases since the average electron density for these planes is fixed, assuming a fixed composition. For example, we found that Pt_3Co/C annealed at 715 °C had a peak ratio of 0.020, and therefore we calculated that the phase fraction of NPs adopting the ordered phase was ~26%.

To better understand the changes in XRD patterns as a function of the annealing temperature, the as-synthesized

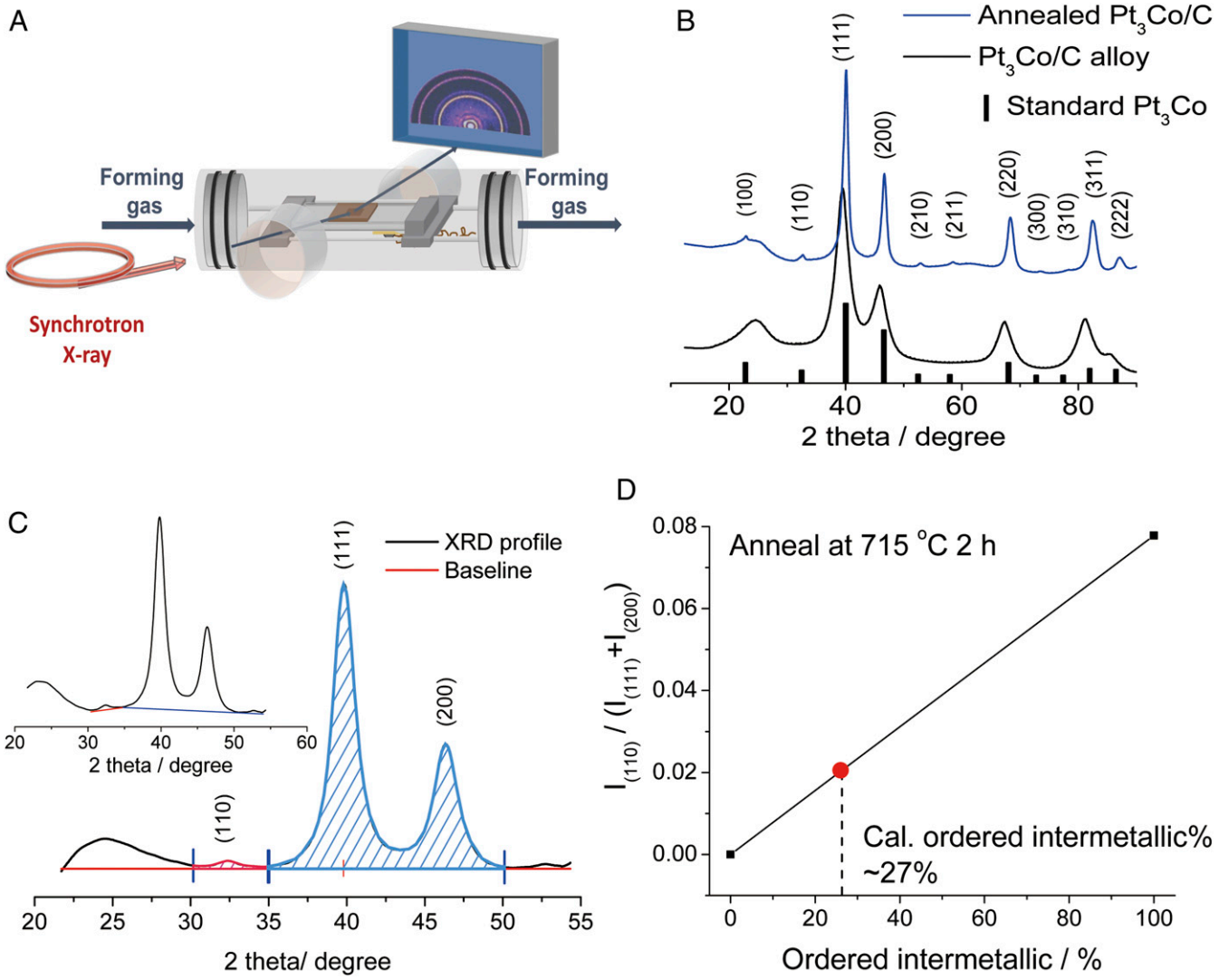

Fig. 1. (*A*) Schematic illustration of the homemade device for the in situ synchrotron-based (XRD study). (*B*) XRD patterns of the as-synthesized Pt_3Co/C alloy and Pt_3Co/C after further annealing at 700 °C in the in-situ heating cell. (*C*) Quantitative analysis of the peak integral of the (110) ordering peak and the (111) and (200) major peaks. (*C, Inset*) Illustration of background subtraction. (*D*) Quantitative calculations of the relative content of ordered intermetallic based on the assumption of a linear relationship between the ratio of the integrated areas of the ordered intermetallic peak at (110) to the sum of the (111) and (200) peaks.

Pt_3Co/C alloy catalysts were annealed at different temperatures, for 2 h each, in flowing forming gas (Fig. 2*A*). After the 2-h anneal, the intensity of the (110) superstructure peak at ~33° was compared with the fundamental (111) reflections. We found that the ratio, $I_{(110)}/(I_{(111)} + I_{(200)})$, increased with annealing temperature over the 600 °C to 750 °C range. The increased ordering is likely due to the enhanced ability to overcome the nucleation and diffusion barriers with increasing temperature. The maximum relative superstructure peak intensity at 750 °C was 0.023, corresponding to an ordered intermetallic phase fraction of about 30%. When annealed at 825 °C for 2 h, the relative fraction of the ordered phase went to zero, within the signal to noise level, consistent with the presence of only the disordered phase which is stable when $T > T_c$ (750 °C) in the bulk Pt-Co phase diagram. Similar changes at different temperatures were also observed in the powder XRD under the same conditions during the postsynthesis annealing treatment in a traditional tube furnace (*SI Appendix*, Fig. S2).

There are several factors that may influence the behavior of an ensemble of particles during annealing. The first is the diffusion rate, both intra- and interparticle, which increases with increasing temperature. Overall, diffusion will drive the composition to be spatially uniform. After sufficient time, all particles will be alike. Concomitantly, the average particle size will grow. Further, higher diffusion rates will allow the NP's to reach their equilibrium state faster. During the cooling process, the driving force for nucleation increases and the diffusion rate decreases as the temperature falls below the phase transition temperature. The next consideration is the stoichiometric ratio of the components (Pt to M). The stoichiometric ratio may vary from particle to particle due to the randomness of aggregation of Pt and M to a growing particle. The average ratio, of course, will be determined by the ratio of reagents used in a particular synthesis procedure. Particle size and morphology may also play a factor in the overall behavior. Finally, even at thermodynamic equilibrium, the degree of ordering will likely be less than 100% due to strain and finite size effects. Since thermal equilibrium is reached by diffusion, low temperature anneals may not result in nucleation nor subsequent growth.

We observed a sharper (111) peak at the higher annealing temperatures (Fig. 2*A*). The average domain size of each ensemble of particles was estimated by the Scherrer equation using the full width at half-maximum of the (111) peak, which is fairly

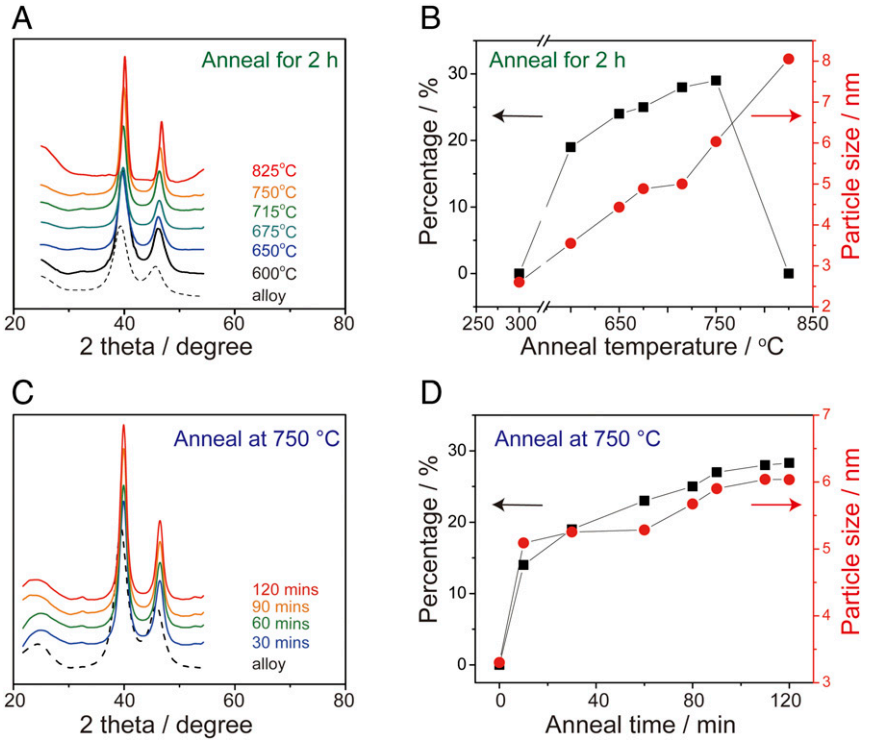

Fig. 2. (*A*) In situ heating XRD patterns of Pt_3Co/C annealed at various temperatures. The dashed line represents the as-synthesized Pt_3Co/C alloy. (*B*) Calculated relative content of ordered intermetallic Pt_3Co/C formed and particle size [calculated from the width of the (111) peak]. (*C*) In situ heating XRD patterns of Pt_3Co/C at 750 °C, the optimal temperature, as a function of annealing time. (*D*) Calculated relative content of ordered Pt_3Co/C formed and particle size.

consistent with the particle size determined from our TEM analysis (*vide infra*). After a 2-h annealing process, the average domain size of Pt_3Co/C increased from 3.5 nm to 6 nm with increasing annealing temperature from 600 °C to 750 °C, and it became as large as 8 nm when the temperature was 825 °C. The (111) diffraction peak also shifted gradually to higher angles, indicating that the corresponding lattice d-spacing decreased from 2.29 Å, before annealing, and reached a value as low as 2.24 Å after a 2 h anneal at 825 °C. The d-spacing approached the theoretical value of ordered bulk Pt_3Co, 2.21 Å (*SI Appendix*, Fig. S3*A*). The relative content of the ordered phase and the particle size, both increased with increasing temperatures when the temperature was 600∼750 °C (Fig. 2*B*). The above behavior is similar to that of bulk $AuCu_3$ and PtCo NPs (38–42).

At 750 °C, which was the optimal annealing temperature for the highest degree of ordering achieved in this experiment, the XRD patterns were tracked dynamically as a function of annealing time (Fig. 2*C*). The (110) ordering peak became more pronounced, and the (111) peak became sharper and shifted to higher angles with longer annealing times. The calculated phase content of ordered Pt_3Co/C and domain sizes exhibited a similar trend: they both increased rapidly during the first half hour, and gradually approached a relatively stable plateau (Fig. 2*D*). This suggested that 2 h was sufficient time to achieve a steady state (or possibly equilibrium) and optimal contents of the ordered phase at such temperatures. After 2 h of annealing at 750 °C, Pt_3Co/C had an average domain size of 6 nm and a (110) ordered peak intensity of 30% relative to the maximum possible, if ordering was complete. In addition, the d-spacing decreased during the first 30 min and approached a plateau (*SI Appendix*, Fig. S3*B*), indicating that the lattice contracted during annealing as the average order increased.

To investigate quantitatively the influence of Pt_3Co particle size (3∼8 nm) on the onset of disorder, we used MC simulations to calculate the degree of substitutional ordering at thermodynamic equilibrium at various temperatures from the average atomic occupation of the lattice sites (38–42). The order–disorder transition (ODT) was characterized by both the long-range order parameter (LROP) and the short-range order parameter (SROP) and plotted as a function of temperature in Fig. 3 for two NP sizes (2.9 and 5.2 nm) and the bulk system (see calculation details in *SI Appendix*). For each system, the temperature at which the LROP and SROP curves exhibit inflection points is roughly the same and marks the ODT temperature, T_{ODT}. At T_{ODT}, the system undergoes a transition from the $L1_2$ phase (Fig. 3*B*) to a disordered phase via an intermediate, transient $D0_{22}$ phase (Fig. 3*C* and Movie S1). The $D0_{22}$ phase also possesses global long-range order with lower crystal symmetry, but is not captured by the LROP used (Fig. 3 *B* and *C*). The T_{ODT} of the NPs is significantly lower than that of the bulk system (750 °C), and there is a clear trend of a decrease in T_{ODT} with a decrease in NP size. This indicates that for a certain range of temperatures (below the bulk T_{ODT}) one could observe larger NPs maintaining higher degree of substitutional order than smaller NPs, which is consistent with our experimental observations in Fig. 2*B*.

To dynamically track the evolution of the superlattice ordering peaks during the annealing process, the XRD patterns of Pt_3Co/C were obtained by increasing the temperature at a very slow rate of 0.5 °C/min from 620 °C to 830 °C (Fig. 4*A*). Because each diffraction scan took less than 2 min, the temperature resolution was within 1 °C. With higher annealing temperatures, the (110) peak became more pronounced and attained a maximum at 720–750 °C, while the absolute intensity of the (111) peak decreased, due to additional disordering in the lattice above the transition temperature as well as to Debye-Waller effects (43, 44). The relative magnitude of the peak intensity ratio of (110) to (111), with the maximum ratio normalized to 100%, was employed as a simple (and reliable) metric to represent the relative amount of the ordered phase (Fig. 4*B*).

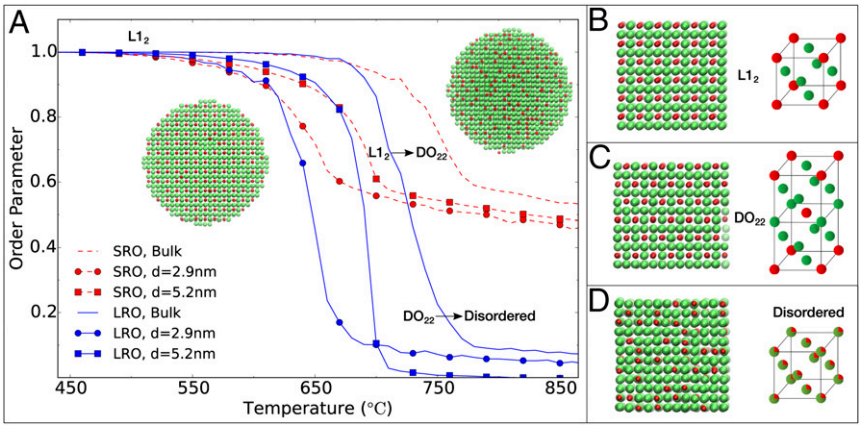

Fig. 3. (*A*) Simulation results for the SROP (red, dashed line) and LROP (blue, solid line) as a function of temperature for bulk (n = 864; no marker) and spherical NPs with diameter (d) = 2.9 nm (n = 800; circles) and d = 5.2 nm (n = 4,800; squares), with snapshots shown at temperatures just before the ODT on the left and just after the ODT on the right. The temperatures are rigidly shifted so as to match the simulation results to the experimental bulk ODT temperature. As the size of the NP is reduced, the ODT temperature for the NPs also decreases. (*B–D*) Snapshots of the bulk trajectory taken at increasing temperatures showing ordered intermetallic phase, $L1_2$ (*B*), $D0_{22}$ state with global long-range order and lower crystal symmetry (*C*), and disordered solid solution phase (*D*). The green and red atoms represent Pt and Co, respectively.

Because the annealing treatment of binary intermetallics during synthesis must be accompanied by cooling of the catalysts down to room temperature, the cooling procedure, after the in situ annealing process, was also investigated. Pt_3Co/C powders, annealed at 715 °C for 2 h were used as a baseline to measure the effect of different cooling rates (*SI Appendix*, Fig. S4*A*). After annealing at 715 °C for 2 h, and cooling to room temperature, the (111) peak shifted to higher angle, indicating that the lattice had contracted further. Cooling experiments were conducted at two different cooling rates after 2 h of annealing (*SI Appendix*, Fig. S4*B*). The first was a slow rate of 6 °C/min, and in the second, the sample was cooled by turning off the electric heater and allowing the gas in the device to cool naturally at a rate of ~30 °C/min. At the slower cooling rate, the relative contents of the ordered Pt_3Co/C phase increased, which was ascribed to the extended period for the atomic rearrangement to the thermodynamically favored state. The sample cooled at a higher rate showed only a slight increase in ordered phase content.

In summary, the effects of the annealing and cooling processes at different annealing temperatures and times on the ordered intermetallic content, were investigated. We conclude that the optimal annealing conditions were to anneal Pt_3Co/C at 750 °C for 2 h and then to cool to room temperature at a slow rate (e.g., 6 °C/min). Other cooling procedures may lead to an even larger fraction of ordered particles. Such processing parameters are used to manufacture heat-resistant CorningWare glass and in toughening metals by age precipitation hardening, for example.

In Situ Heating Scanning TEM. In addition to enabling structured ordering, the thermal annealing process can also alter the morphology of the Pt_3Co NPs. The most important morphological change was coarsening of the Pt_3Co particles, which increased their size and decreased the catalysts' active surface area. To observe these morphological changes, we conducted in situ annealing experiments in a scanning TEM (STEM).

A Pt_3Co/C alloy specimen was annealed at 750 °C for 2 h in an in situ STEM specimen holder in vacuum to approximate the conditions of a typical annealing protocol. Images were acquired alternately in three separate regions of the specimen to provide a more robust and representative measurement of changes in the specimen (Fig. 5 and Movies S2–S4). Fig. 5 *A–C* shows a broad area of the sample before the annealing procedure and after

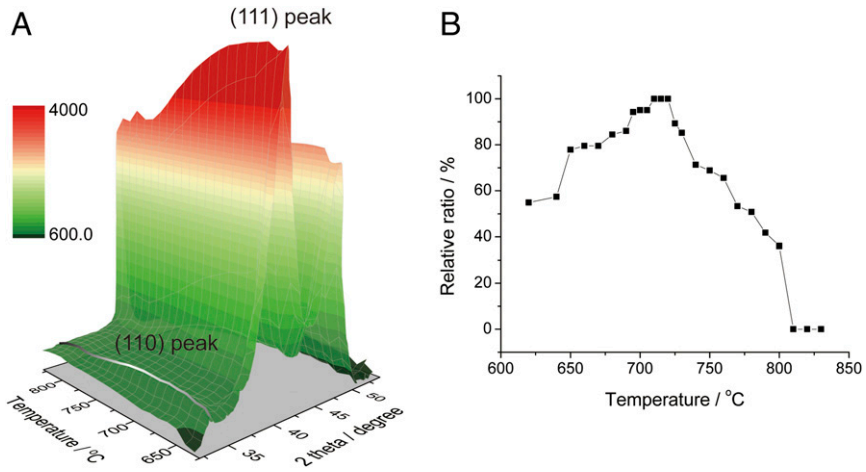

Fig. 4. (*A*) In situ heating XRD patterns of Pt_3Co/C annealed from 620 °C to 830 °C at a slow temperature ramping rate of 0.5 °C/min. (*B*) Relative peak integral ratio of the (110) to (111) peaks (with the maximum ratio normalized to 100%) at a series of temperatures.

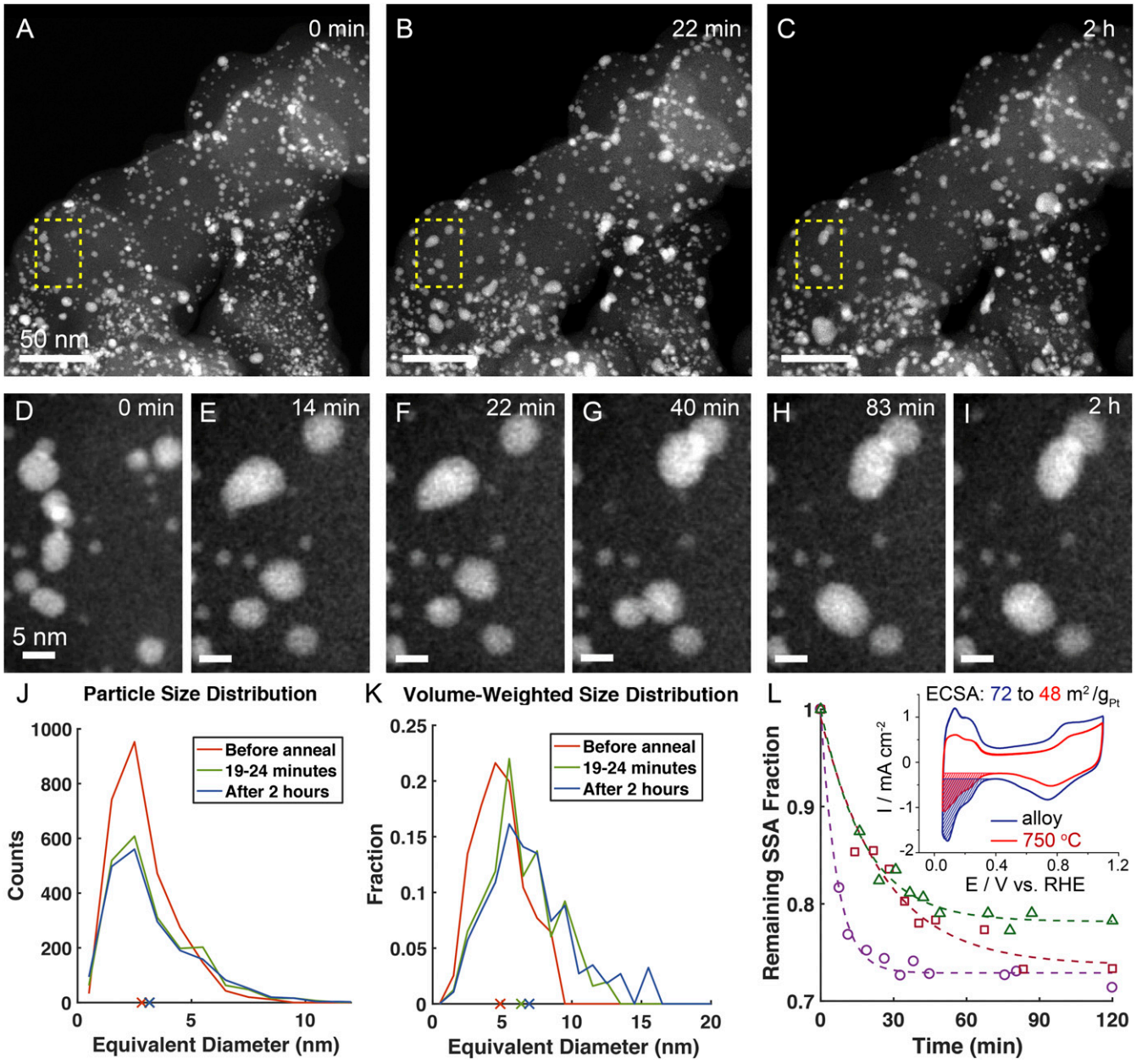

Fig. 5. In situ heating STEM enabling tracking of the morphological changes of Pt_3Co/C annealed at 750 °C. (*A–C*) Pt_3Co/C before annealing (*A*), annealed for 22 min (*B*), and annealed for 2 h (*C*), respectively. (*D–I*) A specific region was magnified to illustrate particle migration and coalescence during a continuous 2-h annealing process. (*J*) Measured distribution of particle sizes of thousands of particles from Fig. 4*A* at different annealing times at 750 °C. Cross marks on the *x* axis represent the corresponding average particle sizes. (*K*) Volume-weighted, particle size distribution, which reflects the relative contribution of larger particles more clearly, as shown by the more pronounced tails for particle sizes above 8 nm. Cross marks on the *x* axis represent the corresponding volume-weighted, average particle sizes. (*L*) SSA (m^2/g_{Pt}) estimated from STEM images of three different regions at different annealing times. (*L*, *Inset*) ECSA for Pt_3Co/C before and after annealing at 750 °C for 2 h, measured from the coulometric charge associate with hydrogen adsorption (H_{ads}) regions in the cyclic voltammograms. Details of statistical analysis of particle sizes and SSA calculations can be found in the experimental section. (Scale bars: *A–C*, 50 nm; *D–I*, 5 nm.) Dynamic changes can be found in Movie S2.

22 min and 2 h of heating at 750 °C, respectively. An overall coarsening of the particles was evident throughout the region, especially during the first 22 min. Fig. 5 *D–I* shows a smaller subregion, in detail, to highlight the observed particle coalescence, which appeared to be the primary coarsening mechanism. Significant particle mobility on the carbon support was also observed, with some particles moving more than 10 nm and growing significantly in size from collisions and coalescence with other particles. Note that several ∼2-nm particles remained fixed near their initial positions throughout the experiment with no noticeable change in size. This observation argues against Ostwald ripening as being a significant contributor to the particle coarsening. Dynamic movements of particles can be seen in the Movie S2.

Additional insights can be gained by calculating the statistical distribution of particle sizes and considering their change during the experiment (Fig. 5*J*). The particle size distribution approximately followed a lognormal form, with smaller 2- to 3-nm particles being the most common with a substantial tail of larger particles. After annealing, the count of smaller particles decreased, while the distribution tail of larger particles grew

more pronounced. This change in the shape of the distribution is also consistent with coarsening by particle coalescence, when a subset of smaller particles merge to form larger particles (45, 46). By contrast, an Ostwald ripening mechanism would have resulted in a more uniform shift in the distribution. The most significant change in the distribution occurred before the end of the 19-to-24-min frame, although more subtle changes in the distribution occurred during the remainder of the annealing process. The growth in the number of large particles is more readily observed in the volume-weighted size distribution (Fig. 5*K*), which shows that larger particles, formed by coalescence, accounted for a significant fraction of the Pt_3Co volume, even though large particles were relatively few in number.

The consequences of coarsening that occurred during the annealing process, on the electrochemical surface area (ECSA) of the Pt_3Co particles were examined by estimating the specific surface area (SSA) of the particles from the images in each region of the specimen (Fig. 5*L*). The overall estimated SSA loss was ~20–30% and it varied among the three different locations in the specimen. This was similar in magnitude to the 33% loss in ECSA that we calculated from the cyclic voltammograms of Pt_3Co/C annealed for 2 h at 750 °C in forming gas as discussed below (Fig. 5*L*, *Inset*). In each specimen region, the SSA tended to decrease in approximately an exponential manner, and decayed toward a lower (but nonzero) value with a time constant that varied from 7 to 25 min among the three different regions. This confirmed previous observations that the most significant changes in the distribution of particle sizes occurred very early in the annealing process. The variation between the total SSA loss and the decay rate likely reflect differences in the strength of the bonding between Pt_3Co particles and the carbon support, suggesting that the structure of the carbon support can be quite heterogeneous.

Atomic-Scale ex Situ High-Angle Annular Dark-Field STEM Imaging. To directly observe the crystal structure of ordered intermetallics at the atomic scale, we employed aberration-corrected STEM to study the Pt_3Co/C after the annealing and cooling processes. We used the high-angle annular dark-field (HAADF) STEM imaging mode, which provides intensities that scale with the atomic number ($I \propto Z^{1.7}$) so that Pt atoms appear much brighter than Co atoms. $L1_2$ intermetallic ordering in Pt_3Co NPs can be recognized by the presence of unique, superlattice-ordered unit cells. The atomic-scale STEM image of a Pt_3Co particle along the [100] zone axis exhibits a periodic square array of dimmer Co atom columns at the center, surrounded by brighter Pt columns at the corners (Fig. 6*A*). The square symmetry is consistent with the projected crystal model along the same [100] zone axis in ordered Pt_3Co intermetallics, where four pure Pt atom columns (red), at the corners, surround the pure Co atom columns (green) at the center (Fig. 6*C*). However, another single-crystal Pt_3Co NP (Fig. 6*B*), which was viewed along the [100] zone axis, exhibited only a partially ordered intermetallic phase, as only parts of the NP showed a similar variation in the intensity as the crystal model suggested (Fig. 6*C*). Other parts of the NP showed atoms at the center that were as bright as atoms at the corners, indicating that only a short-range, atom ordering existed in such Pt_3Co NPs. Fig. 5 *A* and *B* indicate that both fully and partially ordered intermetallics exist in the Pt_3Co NPs after the annealing process.

Correlation of the Degree of Ordering to the Catalyst's Durability. The above mechanistic studies involving both in situ heating XRD and in situ heating TEM yield a fuller picture of the ODPT and provide further practical guidance for the design of ORR catalysts with enhanced durability. The electrochemical properties of the electrocatalysts annealed at different temperatures in a tube furnace were studied systematically to correlate the degree of ordering to the catalyst's durability (Fig. 7). The powder XRD patterns of annealed Pt_3Co/C (*SI Appendix*, Fig. S2) exhibited a similar trend as the in situ heating XRD patterns in Fig. 2. The mass-specific activity (MA), the surface area-specific activity (SA), and the ECSA of the Pt_3Co/C alloy electrocatalysts that were annealed at different temperatures were measured and calculated initially and after stability cycling, which involved potential cycling at 50 mV/s in 0.1 M $HClO_4$ over the potential range of 0.6–1.0 V vs. the reversible hydrogen electrode (RHE). (*SI Appendix*, Figs. S5–S6) Fig. 6*A* presents the ECSA, MA, and SA of Pt_3Co/C annealed at various temperatures. The ECSA exhibited a minimal decrease from 650 to 750 °C while both of MA and SA improved with the degree of ordering and reached a maximum at 750 °C. After stability tests, similar trends in MA and SA were evident However, in all cases, the activity decreased dramatically when the annealing temperature exceeded 750 °C, as would be anticipated. Furthermore, their relative retentions were calculated from the ratio between the initial activity/surface areas to that after the durability tests (Fig. 7*A* and *SI Appendix*, Table S2). With increasing annealing temperature, the retention of the SA and MA improved continuously until reaching the highest values of 94% and 95%, respectively, at 750 °C. However, they

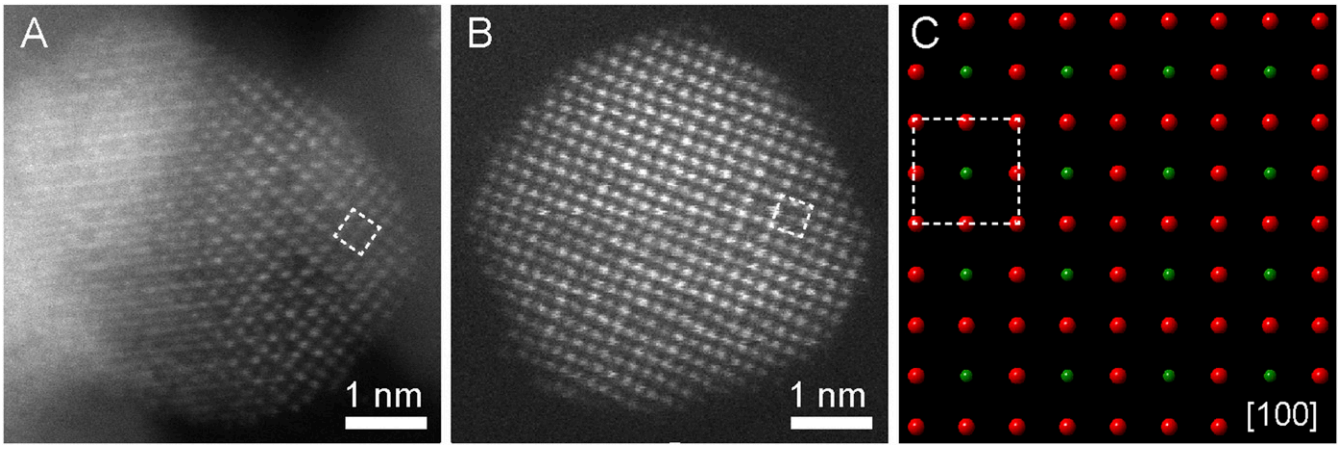

Fig. 6. Atomic-scale ex situ HAADF-STEM images of Pt_3Co/C after annealing. (*A*) An ordered intermetallic Pt_3Co particle on the [100] zone axis. Brighter atoms at corners of squares are Pt, and dimmer atoms at the center are Co. (*B*) A partially ordered intermetallic particle on the [100] zone axis. Both brighter and dimmer atoms exist at the center of the squares. (*C*) Corresponding projected crystal model along [100]. Red and green atoms are Pt and Co, respectively. Crystal models were built based on the ordered intermetallic Pt_3Co (PDF #01-071-7410).

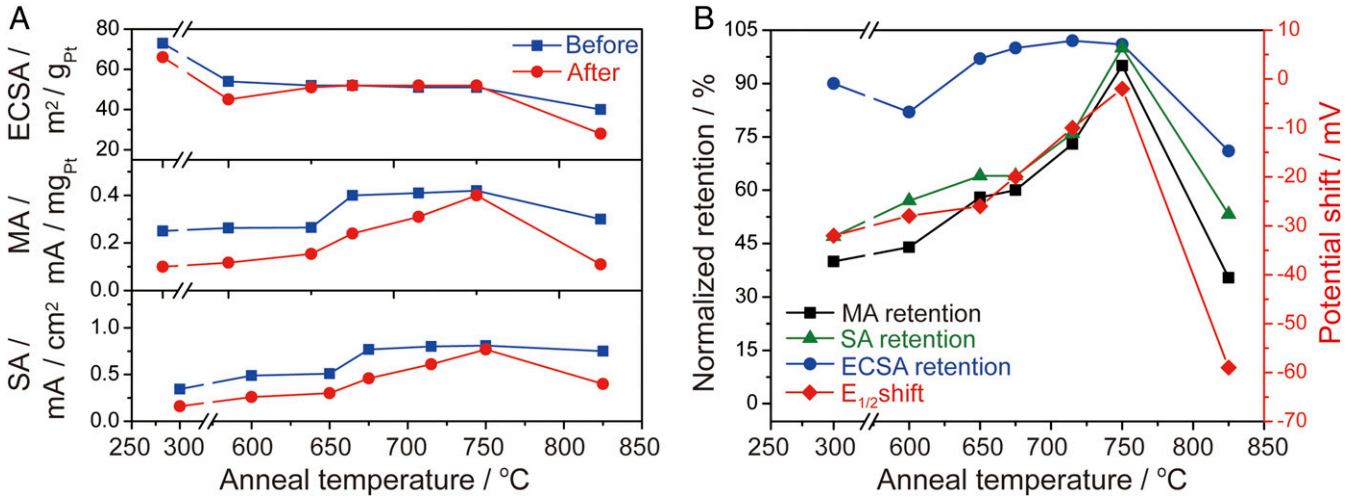

Fig. 7. (*A*) Calculated ECSA, MA, SA at 0.9 V vs. RHE of Pt_3Co/C before and after stability tests, after a series of annealing temperatures for 2 h. (*B*) Normalized retention of MA, SA, and ECSA on the left axis and half-wave potential shift on the right axis of Pt_3Co/C after annealing at different temperatures. Normalized retention was calculated based on the ratio of the initial activity/surface areas to that after durability tests (2,000 cycles in cyclic voltammetry at 100 mV/sec in 0.1 M $HClO_4$ over the potential at the range from 0.6 to 1.0 V vs. RHE). The best durability was achieved at around 750 °C, corresponding to the optimal degree of ordering.

dramatically decreased when the annealing temperature was increased to 825 °C. The trends in retention of SA and MA were quite consistent with the degree of ordering of the intermetallics, which indicated that the more ordered atomic structure improved the durability of the Pt_3Co/C NPs. ECSA retention reached a maximum plateau at 725–750 °C with nearly no decay, with respect to its initial value, suggesting that a higher degree of ordering suppressed the loss of Pt surface area. It should be noted that the as-synthesized Pt_3Co/C (reduced at 300 °C) had a slightly higher ECSA than Pt_3Co/C that was annealed at 600 °C, likely because the as-synthesized Pt_3Co/C contained particles that were smaller than those annealed at 600 °C. This may have counteracted, or even surpassed, the benefit of the higher degree of ordering at 600 °C.

The shift in the half-wave potential ($E_{1/2}$), which is considered as an indicator of the intrinsic electrocatalytic activity in a more straightforward way, was also evaluated for its stability. The $E_{1/2}$ exhibited a trend similar to the SA and MA, with the least negative shift (<5 mV) observed at the optimal annealing temperature of 750 °C. The improvement in the stability of the Pt_3Co with the highest ordered degree comes from the stable intermetallic Pt, Co arrangement in the core and the Pt rich shell. In the stability test of Pt_3Co alloy or intermetallics, the degradation of the electrocatalyst comes mainly from the loss of Co and the leached Co ions in the electrolyte, in turn contaminating the Pt surface. The intermetallic NP with the highest ordered degree had the most uniform and regular atomic structure, so the Co was mostly bonded and surrounded by Pt. Also, the stable and ordered

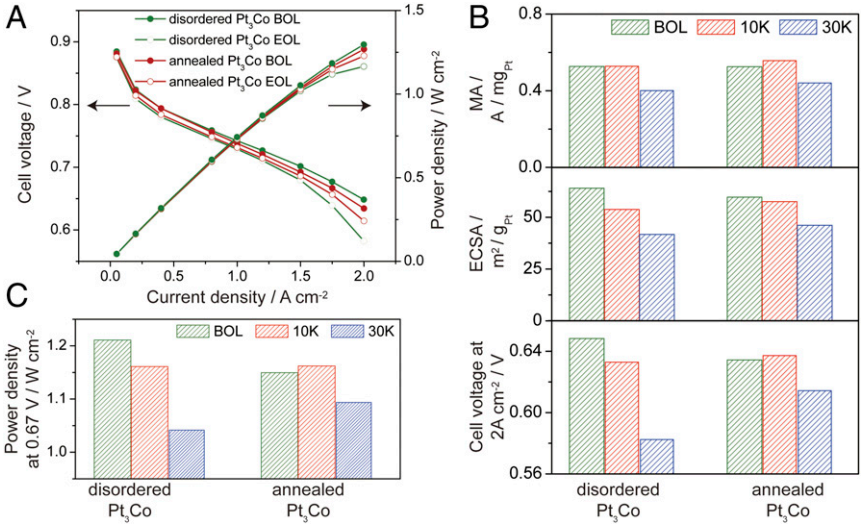

Fig. 8. Fuel cell performance comparison of disordered and annealed Pt_3Co/C before and after stability testing. BOL and EOL represent beginning-of-life (initial performance) and end-of-life (after 30,000 cycles), respectively. (*A*) MEA performance at Pt loadings of 0.025 and 0.10 mg_{Pt}/cm^2 on anode and cathode, respectively. Cell operation conditions are in the order of anode/cathode: H_2/air, 94 °C, 65/65%RH, 250/250 $kPa_{abs,outlet}$, stoichiometries of 1.5/2. (*B*) MA measured at 0.9 V vs. RHE (*Upper*), ECSA of Pt measured by CO stripping in MEA (*Middle*), and voltage measured at a high current density of 2 A/cm^2 (*Lower*). (*C*) Power density at 0.67 V under the same condition as *A*.

structure maintained the robust atomic structure, retaining the highest ECSA after the cycling process. As a result, it yielded a large improvement in the $E_{1/2}$ during the stability test. This enhancement is not only observed from the RDE experiments but also demonstrated in the membrane-electrode assembly (MEA) results (see below). This study represents a successful attempt to systematically correlate the degree of ordering of binary alloy catalysts to the durability of electrocatalysts toward the ORR in fuel cells, which will provide valuable insights and strategies in the future design of novel, ordered intermetallic electrocatalysts.

Real-World Stability Evaluation. For practical applications in proton-exchange membrane fuel cells (PEMFCs), it is important to confirm that the findings in the laboratory can be translated to real-world (practical) improvement. The annealed, ordered, Pt_3Co/C electrocatalysts prepared in this work were evaluated in a fuel cell MEA and compared with one of the most active and durable state-of-the-art PtCo/C catalysts (Fig. 8) (7, 47). The disordered Pt_3Co/C used for comparison was made by chemically dealloying a PtCo/C precursor. The disordered Pt_3Co/C had already exhibited excellent activity and stability in MEA results and had surpassed the US Department of Energy (DOE) targets (initial ORR mass activity >0.44 A/mg_{Pt} and <40% loss after stability test) (Fig. 8*B*). In this study, the disordered Pt_3Co was further processed through the aforementioned optimal annealing conditions to achieve a maximum degree of ordering. The annealed Pt_3Co/C showed comparable initial ORR activity and Pt ECSA to the disordered catalyst; however, it had about a 40% lower loss after the stability test (Fig. 8*B*, *Middle*). This is an impressive achievement over an already-very-stable, high performing electrocatalyst. These results support the findings of the above-described in situ experiments on Pt_3Co, that ordered intermetallic phases represent a promising path to develop stable, high-performance fuel cell electrocatalysts. The initial high-current-density (HCD) performance (Fig. 8*B*, *Lower* and Fig. 8*C*) of the ordered catalyst, although quite respectable by industry standards, is still slightly lower than our well-optimized baseline disordered Pt_3Co/C catalyst. The development of MEA electrodes for HCD for new catalysts generally takes several months and large amount of materials to optimize the ionomer, catalyst, and pore distribution within the electrode. Taking the mass activity and ECSA of the ordered catalyst into account, we predict that once optimized, the initial performance of the ordered phase Pt_3Co electrocatalyst will surpass that of the disordered Pt_3Co/C catalyst (48).

The greatest value of the stability improvement of this catalyst is especially evident at HCD, as the durability under HCD performance is the leading factor determining the cost of a fuel cell stack (48). The annealed Pt_3Co/C catalyst showed significantly smaller losses compared with the disordered catalyst after 30,000 cycles; only 20 mV vs. 66 mV (Fig. 8*B*, *Lower*). This is due to the better retention of ORR activity and ECSA of the ordered catalysts as discussed above. To practically meet the US Department of Energy (DOE) heat rejection target ($Q/\Delta T$ of <1.45), the voltage must be higher than the 0.67 V under the operating conditions used in this work (94 °C) (47). As shown in Fig. 8*C*, the annealed Pt_3Co/C exhibited only a 5% loss in power density at 0.67 V after 30,000 cycles, relative to a 14% loss for the disordered Pt_3Co/C electrocatalyst. To the best of our knowledge, these results represent a cathode catalyst in PEMFCs with the highest performance and stability published to date. While we employed an accelerated stability test and yet require performing a long-term durability validation in this study, the advancement projects progress toward meeting the US DOE durability target of less than 10% performance loss after 8,000 h of automotive drive cycle.

Conclusions

In summary, this work represents that both in situ heating synchrotron-based XRD for large ensembles of NPs and in situ heating TEM at the microscopic level have been used to quantitatively study the dynamics of the ODPT and morphological and structural changes of binary intermetallics during a thermal annealing treatment. We have studied the impact of the annealing temperature and cooling conditions (temperature and time) comprehensively, on the degree of ordering, particle size, and lattice strain of Pt_3Co intermetallics. Through MC simulations, we have also found that Pt_3Co NPs have a lower ODPT temperature than their bulk counterpart (by up to ~100 °C for 3–5 nm NPs). At the optimal annealing temperature (750 °C), the total content of ordered intermetallic phase peaks at about 30%, reflecting the presence of both fully and partially ordered NPs and a correlation between intermetallic order and particle size. To directly visualize the morphological and structural transitions during the annealing treatment, we further employed in situ heating STEM to study the mechanism of NP migration and growth, and we quantitatively investigated the evolution of particle size distribution and the SSA during the annealing process. We achieved a direct visualization of both fully ordered and partially ordered individual Pt_3Co NPs at the atomic scale. Finally, we have built a structure–activity correlation in which the Pt_3Co/C catalysts, with a higher degree of ordering, exhibited significantly enhanced durability. We further demonstrated that the annealed Pt_3Co/C with optimal degree of ordering exhibited remarkable long-term durability in practical MEA measurements in PEMFCs. This systematic and in-depth study, which involved both in situ heating XRD and in situ heating TEM, will have a broad impact on the further development of ordered intermetallic electrocatalysts for fuel cell applications.

ACKNOWLEDGMENTS. We thank Dr. Arthur Woll and Dr. Stanislav Stoupin for their assistance in setting up beamline hardware and guidance in XRD analysis. We appreciate the assistance of Michael K. Carpenter (General Motors) in MEA measurements. We thank Prof. Thomas Gavin (Cornell University) for his help in editing the manuscript. This work used TEM facilities of the Cornell Center for Materials Research, which was supported through the National Science Foundation (NSF) Materials Research Science and Engineering Center program (NSF Awards DMR-1429155 and DMR-1719875). This work was primarily supported by the US DOE's Office of Energy Efficiency and Renewable Energy Grant DE-EE0007271. The in situ XRD work was based on research conducted at CHESS, which was supported by NSF Award DMR-1332208.

1. Cano ZP, et al. (2018) Batteries and fuel cells for emerging electric vehicle markets. *Nat Energy* 3:279–289.
2. Wang D, et al. (2013) Structurally ordered intermetallic platinum-cobalt core-shell nanoparticles with enhanced activity and stability as oxygen reduction electrocatalysts. *Nat Mater* 12:81–87.
3. Stamenkovic VR, et al. (2007) Trends in electrocatalysis on extended and nanoscale Pt-bimetallic alloy surfaces. *Nat Mater* 6:241–247.
4. Cui C, Gan L, Heggen M, Rudi S, Strasser P (2013) Compositional segregation in shaped Pt alloy nanoparticles and their structural behaviour during electrocatalysis. *Nat Mater* 12:765–771.
5. Shao M, Chang Q, Dodelet JP, Chenitz R (2016) Recent advances in electrocatalysts for oxygen reduction reaction. *Chem Rev* 116:3594–3657.
6. Xiong Y, Yang Y, DiSalvo FJ, Abruña HD (2018) Pt-decorated composition-tunable Pd–Fe@Pd/C core–shell nanoparticles with enhanced electrocatalytic activity toward the oxygen reduction reaction. *J Am Chem Soc* 140:7248–7255.
7. Han B, et al. (2015) Record activity and stability of dealloyed bimetallic catalysts for proton exchange membrane fuel cells. *Energy Environ Sci* 8:258–266.
8. DeSario DY, DiSalvo FJ (2014) Ordered intermetallic Pt–Sn nanoparticles: Exploring ordering behavior across the bulk phase diagram. *Chem Mater* 26:2750–2757.
9. Yan Y, et al. (2017) Intermetallic nanocrystals: Syntheses and catalytic applications. *Adv Mater* 29:1605997.
10. Luo M, Sun Y, Wang L, Guo S (2017) Tuning multimetallic ordered intermetallic nanocrystals for efficient energy electrocatalysis. *Adv Energy Mater* 7:1602073.
11. Abe H, et al. (2008) Electrocatalytic performance of fuel oxidation by Pt_3Ti nanoparticles. *J Am Chem Soc* 130:5452–5458.
12. Cui Z, et al. (2014) Synthesis of structurally ordered Pt_3Ti and Pt_3V nanoparticles as methanol oxidation catalysts. *J Am Chem Soc* 136:10206–10209.
13. Ghosh T, Leonard B, Zhou Q, DiSalvo FJ (2010) Pt alloy and intermetallic phases with V, Cr, Mn, Ni, and Cu: Synthesis as nanomaterials and possible applications as fuel cell catalysts. *Chem Mater* 22:2190–2202.

14. Kang Y, Murray CB (2010) Synthesis and electrocatalytic properties of cubic Mn-Pt nanocrystals (nanocubes). *J Am Chem Soc* 132:7568–7569.
15. Chung DY, et al. (2015) Highly durable and active PtFe nanocatalyst for electrochemical oxygen reduction reaction. *J Am Chem Soc* 137:15478–15485.
16. Leonard B, Zhou Q, Wu D, DiSalvo FJ (2011) Facile synthesis of PtNi intermetallic nanoparticles: Influence of reducing agent and precursors on electrocatalytic activity. *Chem Mater* 23:1136–1146.
17. Wang D, et al. (2012) Tuning oxygen reduction reaction activity via controllable dealloying: A model study of ordered Cu_3Pt/C intermetallic nanocatalysts. *Nano Lett* 12:5230–5238.
18. Chen Q, et al. (2014) Wet chemical synthesis of intermetallic Pt_3Zn nanocrystals via weak reduction reaction together with UPD process and their excellent electrocatalytic performances. *Nanoscale* 6:7019–7024.
19. Kang Y, Pyo JB, Ye X, Gordon TR, Murray CB (2012) Synthesis, shape control, and methanol electro-oxidation properties of Pt-Zn alloy and Pt_3Zn intermetallic nanocrystals. *ACS Nano* 6:5642–5647.
20. Miura A, Wang H, Leonard B, Abruña HD, DiSalvo FJ (2009) Synthesis of intermetallic PtZn nanoparticles by reaction of Pt nanoparticles with Zn vapor and their application as fuel cell catalysts. *Chem Mater* 21:2661–2667.
21. Wang X, et al. (2013) Pt/Sn intermetallic, core/shell and alloy nanoparticles: Colloidal synthesis and structural control. *Chem Mater* 25:1400–1407.
22. Kuttiyiel KA, et al. (2014) Gold-promoted structurally ordered intermetallic palladium cobalt nanoparticles for the oxygen reduction reaction. *Nat Commun* 5:5185.
23. Li G, et al. (2014) An ordered bcc CuPd nanoalloy synthesised via the thermal decomposition of Pd nanoparticles covered with a metal-organic framework under hydrogen gas. *Chem Commun (Camb)* 50:13750–13753.
24. Jiang K, et al. (2016) Ordered PdCu-based nanoparticles as bifunctional oxygen-reduction and ethanol-oxidation electrocatalysts. *Angew Chem Int Ed Engl* 55: 9030–9035.
25. Cable R, Schaak R (2007) Solution synthesis of nanocrystalline M-Zn (M: Pd, Au, Cu) intermetallic compounds via chemical conversion of metal nanoparticle precursors. *Chem Mater* 19:4098–4104.
26. Gunji T, et al. (2017) Enhanced electrocatalytic activity of carbon-supported ordered intermetallic palladium–lead (Pd_3Pb) nanoparticles toward electrooxidation of formic acid. *Chem Mater* 29:2906–2913.
27. Chen W, et al. (2010) A seed-based diffusion route to monodisperse intermetallic CuAu nanocrystals. *Angew Chem Int Ed Engl* 49:2917–2921.
28. Wang G, et al. (2014) Pt skin on AuCu intermetallic substrate: A strategy to maximize Pt utilization for fuel cells. *J Am Chem Soc* 136:9643–9649.
29. Sra AK, Schaak RE (2004) Synthesis of atomically ordered AuCu and $AuCu_{(3)}$ nanocrystals from bimetallic nanoparticle precursors. *J Am Chem Soc* 126:6667–6672.
30. Okamoto H (2001) Co-Pt (cobalt-platinum). *J Phase Equilib* 22:591.
31. Oezaslan M, Hasché F, Strasser P (2011) *In situ* observation of bimetallic alloy nanoparticle formation and growth using high-temperature XRD. *Chem Mater* 23: 2159–2165.
32. Avanesian T, et al. (2017) Quantitative and atomic-scale view of CO-induced Pt nanoparticle surface reconstruction at saturation coverage via DFT calculations coupled with *in situ* TEM and IR. *J Am Chem Soc* 139:4551–4558.
33. van der Vliet DF, et al. (2012) Mesostructured thin films as electrocatalysts with tunable composition and surface morphology. *Nat Mater* 11:1051–1058.
34. Dubau L, et al. (2016) Defects do catalysis: CO monolayer oxidation and oxygen reduction reaction on hollow PtNi/C nanoparticles. *ACS Catal* 6:4673–4684.
35. Dai S, et al. (2017) In situ atomic-scale observation of oxygen-driven core-shell formation in Pt_3Co nanoparticles. *Nat Commun* 8:204.
36. Chi M, et al. (2015) Surface faceting and elemental diffusion behaviour at atomic scale for alloy nanoparticles during *in situ* annealing. *Nat Commun* 6:8925.
37. Xin HL, et al. (2014) Revealing the atomic restructuring of Pt-Co nanoparticles. *Nano Lett* 14:3203–3207.
38. Alloyeau D, et al. (2009) Size and shape effects on the order-disorder phase transition in CoPt nanoparticles. *Nat Mater* 8:940–946.
39. Keating DT, Warren BE (1951) Long-range order in beta-brass and Cu_3Au. *J Appl Phys* 33:286–290.
40. Yasuda H, Mori H (1996) Effect of cluster size on the chemical ordering in nanometer-sized Au-75at%Cu alloy clusters. *Z Phys D* 37:181–186.
41. Front A, Legrand B, Trélia G, Mottet C (2019) Bidimensional phases in Co–Pt surface alloys: A theoretical study of ordering and surface segregation. *Surf Sci* 679:128–138.
42. Rosato V, Guillope M, Legrand B (1989) Thermodynamical and structural properties of f.c.c. transition metals using a simple tight-binding model. *Philos Mag A* 59:321–336.
43. Warren BE (2014) *X-Ray Diffraction* (Dover Publications, New York).
44. Flinn P, McManus G, Rayne J (1961) Effective X-ray and calorimetric Debye temperature for copper. *Phys Rev* 123:809–812.
45. Granqvist CG, Buhrman RA (1976) Size distributions for supported metal catalysts: Coalescence growth versus Ostwald ripening. *J Catal* 42:477–479.
46. Xin HL, et al. (2012) Atomic-resolution spectroscopic imaging of ensembles of nanocatalyst particles across the life of a fuel cell. *Nano Lett* 12:490–497.
47. Yarlagadda V, et al. (2018) Boosting fuel cell performance with accessible carbon mesopores. *ACS Energy Lett* 3:618–621.
48. Kongkanand A, Mathias MF (2016) The priority and challenge of high-power performance of low-platinum proton-exchange membrane fuel cells. *J Phys Chem Lett* 7: 1127–1137.